Lawrence Berkeley National Laboratory
LBL Publications

Title

Chemical Environment and Structural Variations in High Entropy Oxide Thin Film Probed with Electron Microscopy

Permalink

https://escholarship.org/uc/item/38w6b0f4

Journal

ACS Nano, 18(23)

ISSN

1936-0851

Authors

Miao, Leixin

Sivak, Jacob T

Kotsonis, George

et al.

Publication Date

2024-06-11

DOI

10.1021/acsnano.4c00787

Chemical Environment and Structural Variations in High Entropy Oxide Thin Film Probed with Electron Microscopy

Leixin Miao[1], Jacob T. Sivak[2], George N. Kotsonis[1], Jim Ciston[3], Colin Ophus[3], Ismaila Dabo[1], J.P. Maria[1], Susan B. Sinnott[1] and Nasim Alem[1]*

[1] Department of Materials Science and Engineering, The Pennsylvania State University, University Park, PA, 16802, USA

[2] Department of Chemistry, The Pennsylvania State University, University Park, PA, 16802, USA

[3] NCEM, Molecular Foundry, Lawrence Berkeley National Laboratory, Berkeley, California 94720, United States

ABSTRACT

We employ analytical transmission electron microscopy (TEM) to correlate the structural and chemical environment variations within a stacked epitaxial thin film of the high entropy oxide (HEO) $Mg_{0.2}Co_{0.2}Ni_{0.2}Cu_{0.2}Zn_{0.2}O$ (J14), with two layers grown at different substrate temperatures (500°C and 200°C) using pulsed laser deposition (PLD). Electron diffraction and atomically resolved STEM imaging reveal the difference in out-of-plane lattice parameters in the stacked thin film, which is further quantified at a larger scale using four-dimensional STEM (4D-STEM). In the layer deposited at lower temperature, electron energy loss spectroscopy (EELS) mapping indicate drastic changes in oxidation states and bonding environment for Co ions and energy dispersive X-ray spectroscopy (EDX) mapping detects more significant cation deficiency. Ab-initio density functional theory (DFT) calculations validate that vacancies on the cation sublattice of J14 result in significant electronic and structural changes. The experimental and computational analysis indicates that low temperatures during film growth result in cation deficiency, an altered chemical environment, and reduced lattice parameters while maintaining a single phase. Our results demonstrate that the complex correlation of configurational entropy, kinetics, and thermodynamics can be utilized for accessing a range of metastable configurations in HEO materials without altering cation proportions, paving the path for further engineering of novel functional properties of HEO materials.

INTRODUCTION

Advanced materials have greatly benefited the progress of the fundamental science frontier and technological innovations towards real-world applications. However, identifying the rich source of the new materials has been a constant challenge. More recently, a new frontier of materials discovery, high-entropy (HE) materials, has been initiated to overcome this challenge. These HE materials utilize configurational entropy to stabilize multiple elements into a single lattice (entropy stabilization), enabling nearly unlimited opportunities to discover new materials.[1]

The concept of the HE materials was first realized in metallurgy as equiatomic multicomponent alloys, in which the five constituent metal elements are stabilized into a single-phase alloy.[2] Later, it was found that the single-phase formation can be related to the increased configurational entropy caused by its multiple constituent elements and the equimolar proportions of the elements.[3] Later, the HE concept was further expanded into non-metallic crystalline systems when Rost et al. first experimentally demonstrated the entropy stabilization in the rocksalt phase high entropy oxide (HEO) materials, with the composition of $(Mg_{0.2}Co_{0.2}Ni_{0.2}Cu_{0.2}Zn_{0.2})O$.[4] This rocksalt phase HEO material was designated as the J14 compound, and we will continue using the original terminology in this work. The schematic of its rocksalt crystal structure is shown in Figure 1a. After the successful synthesis of the rocksalt phase HEO, numerous non-metallic HE crystalline materials with distinct compositions and crystal structures have been proposed and studied, such as spinel phase HEO[5], perovskite phase HEO[6], fluorite phase HEO[7], HE carbides[8], HE nitrides[9], HE chalcogenides[10], and many more. Many promising functional properties have been widely reported in HE materials. For example, rocksalt HEO have showed potential fast ionic conduction and reversible ion storage suitable for electrochemical applications, while HE chalcogenides have

exhibited good performance for carbon dioxide electrocatalysis and thermoelectric applications.[10–15]

The entropic stabilization in the HEOs subsequently leads to inherent metastability at low temperatures, where phase separation and chemical segregation are more likely to occur.[4,16,17] In addition, the synthesis conditions, such as the thermal history during growth, growth rate, and oxygen partial pressure, may lead to complicated microstructures and altered physical properties of the HEO crystals.[18–21] These impacts from the synthesis conditions are prominent in the HEO thin films grown with the pulsed laser deposition (PLD) method due to its nonequilibrium growth mechanism. For example, the highly misfit Sc, Ga, and Ca atoms can only be incorporated into the single-phase rocksalt phase HEO thin film using PLD synthesis.[22] the phase structure of Sc-containing HEO thin films can depend on ablated particle kinetic energies, partial oxygen pressure, and growth rate.[19,21] Furthermore, we observed a collective optical, magnetic, and structural properties variation in PLD grown J14 thin films as a function of substrate temperature during synthesis.[18] Our previous study mainly discussed the macroscopic properties of the HEOs affected by the growth conditions, while in this work we further focus on structural and chemical changes at the nanoscale.

Here, we employ advanced electron microscopy techniques to investigate the impact on the structure and chemical environment due to varied growth temperatures in a stacked J14 HEO thin film prepared with PLD. Unsupervised machine learning algorithms are applied to the atomic resolution high angle annular dark-field (HAADF) scanning transmission electron microscopy (STEM) images, which highlights the structural change due to the different growth temperatures. We then utilize four-dimensional scanning transmission electron microscopy (4D-STEM) for large-scale strain measurements and quantified the sizeable out-of-plane strain variations in the

stacked film due to the changes in growth temperature. Monochromated electron energy loss spectroscopy (mono-EELS), assisted by unsupervised machine learning methods, is performed to determine the electronic structure of the oxygen and constituent cations. A drastic change in the chemical environment for Co ions is uncovered while no difference was evident in other cation elements. First-principle calculations support our claim that cation vacancies coincide with an altered chemical environment for primarily Co ions as well as significant changes in unit cell volume.

RESULTS AND DISCUSSION

To control the variables for this investigation and ensure self-consistent characterization, we synthesized a stacked J14 HEO thin film on an MgO substrate. The schematic of the sample is shown in Figure 1b. The first layer of J14 (500°C J14) was deposited at a substrate temperatures of 500°C, and a second layer of J14 (200°C J14) was promptly deposited on top after cooling the substrate to 200°C. Figure 1c shows a low magnification HAADF STEM image that captured the MgO substrate and the stacked J14 layers, and Figure 1d-l shows the simultaneously acquired energy dispersive X-ray spectroscopy (EDX) elemental mapping of the constituent elements. The EDX map indicates the homogenous distribution of the constituent elements within two parts of the stacked film, while the line-averaged intensity profile shows more cation vacancies in the 200°C J14 than in 500°C J14 (Figure 1j). Additionally, there is a slight excess of Cu and a slight deficiency of Mg, Co, Ni, and Zn at the 200°C/500°C J14 interface. We suspect the Cu enrichment at the interface is due to the migration of some Cu ions between layer growths, since the present temperatures are not high enough to balance the positive enthalpy associated with keeping Cu homogeneously dispersed in the rocksalt phase matrix.[4,17] Despite the slight accumulation of Cu at the interface, the epitaxial rocksalt structure is maintained throughout the film stack.

To examine the structural impact of the growth temperature, we investigated the reciprocal space using selected area electron diffraction (SAED). The SAED pattern from the [100] zone axis taken on the stacked film and the substrate is shown in Figure 2a. After close inspection, we did not find any extra peaks indicating a secondary phase. However, we observed a tetragonal distortion of the rocksalt phase as the 006 reflection is split into three distinct spots while the 060 reflection remains a single sharp peak. The magnified images of the 006 and 060 reflections are shown in Figure 2b and 2c. The split of the 006 reflection and the sharp 060 reflection suggest that compared to the MgO substrate, the stacked J14 thin films show expansion and shrinkage in the out-of-plane lattice parameters and the constant in-plane lattice parameters, respectively.

We have acquired and analyzed the high-resolution ADF-STEM images at atomic resolution to examine the structural differences across the stacked J14 thin film interface. To highlight the structural changes, we applied the physics-based deep data image analysis via the unsupervised machine learning algorithm to extract the local distortion from the atomically resolved imaging data.[23,24] In this algorithm, the local crystallography information is extracted via a Fourier transformation (FT) inside a local window on the image. The local window is shifted across the entire image and generates a stack of 2D-FT patterns, which results in four-dimensional spectral image data. The unsupervised machine learning algorithm was then performed on the 2D-FT pattern stack for dimensionality reduction and data clustering. The data clustering results in the automatic image segmentation based on the local crystallographic information. The detailed algorithm for this analysis is listed in the method section and Figure S1. The atomically resolved ADF-STEM image and the image segmentation results across the J14 stacked thin film interface are shown in Figure 2d and 2e. In Figure 2e, each colored spot is the center of the window where the local FT patterns are extracted. The algorithm automatically categorizes the STEM image into

two classes indicated by the blue and red colors, and the corresponding class averaged FT patterns from the blue and red classes are shown in Figures 2f and 2g. As shown in Figure 2e, the FT patterns in the blue and red classes are primarily located in the 200°C and 500°C J14, respectively. The class averaged FT pattern difference highlights the structural difference shown in Figure 2h. The $\vec{g} = 002$ is smaller in magnitude for the red class than the blue class, indicating a larger lattice parameter for the 500°C J14 thin film. The physics-based deep data image analysis results presented here further motivated the 4D-STEM study for a larger scale and high-precision quantification of the lattice parameter differences in the J14 stacked thin films.

Figure 3a shows the 4D-STEM experimental setup schematic with the patterned condenser aperture. In the 4D-STEM experiment, a full 2D nanobeam electron diffraction pattern (NBED, in reciprocal space, u and v) is captured at each scanning position (in real space, x, and y), resulting in a four-dimensional data set containing abundant structural information. The virtual ADF-STEM image of the scanning region is shown in Figure 3b, and the examples of the patterned NBED are shown in Figure 3c-d. The green and yellow spots mark the probe positions in Figure 3b, and the corresponding NBED patterns are acquired from carbon deposition and J14 thin film, shown in Figure 3c and 3d, respectively. The post-acquisition data processing for 4D-STEM enables quantification of large scale (in μm) combined with high precision (in pm) for the strain/lattice parameter measurement by determining the distance between the center of the transmitted beam and the diffracted disks in each NBED pattern. In addition, we used the patterned condenser aperture to further boost the measurement precision for forming the NBED with patterned diffraction disks.[25] The features in the diffraction disks improve the accuracy of the template matching algorithm for the strain measurement and can minimize the impact from the off-axis tilt and dynamic scattering.[25]

Figure 3d contains the results of the 4D-STEM strain mapping performed on the J14 stacked thin film. The reference region is selected on the MgO substrate as shown in the dashed box on the virtual ADF-STEM image in Figure 3b. The strain mapping results are plotted in colored maps with red and blue indicating tensile and compressive strain, respectively. The line averaged strain profiles are plotted on the side of the strain maps. The measurement shows that the differences in in-plane (ε_{xx}), shear (ε_{xy}), and rotation (ω) components are relatively small. On the other hand, there is a significant change of approximately -1% and +1% in out-of-plane (εyy) strain components in 200°C and 500°C J14 thin film on average, respectively. The 4D-STEM results confirmed our previous observation from the SAED and ADF-STEM data and further quantified the large-scale strain profile from the stacked J14 thin film. Furthermore, the strain mapping showed the dislocation at the interface between J14 thin film and MgO substrate (black arrows in Figure 3d), while no dislocation is found at the interface between 500°C and 200°C J14 thin film. To understand the discrepancy for the lattice parameter in the J14 thin films grown at different substrate temperatures, EELS is employed to investigate into the underlying chemical environment changes.

In EELS, the fast electrons interact with the sample and lose energy due to the excitation of the electrons into unoccupied states in the conduction bands. In the high energy loss range, the ionization edges are formed due to the excitation of the electrons at the core level. Furthermore, the EELS setup with sufficient energy resolution can resolve the variation of the intensity and structure for the ionization edges within 30 eV of the edge onset, referred to as the energy loss near edge structure (ELNES). ELNES provides rich information regarding the oxidation states and local chemical environment. We performed mono-EELS measurement in STEM mode (STEM-EELS) at approximately the same region as the 4D-STEM scan on the J14 stacked thin film to resolve the

ELNES for the core loss ionization edge and link the features in the spectra with their spatial locations. In STEM-EELS mode, an EELS spectrum was acquired at each probe position and generated a 3-Dimensional spectral image. The recent advances in the data-driven analysis for EELS, such as unsupervised machine learning methods, enabled spectra unmixing, enhancement and categorization without prior knowledge.[26–29] We applied the unsupervised machine learning algorithm on STEM-EELS data for data categorization by using the dimensionality reduction on the 3D STEM-EELS data with the non-negative matrix factorization (NMF) combined with t-distributed stochastic neighbor embedding (t-SNE).[30] We then applied the gaussian mixture model (GMM) for data clustering. The unsupervised learning assisted STEM-EELS for O k edge results are plotted in Figure 4.

Figure 4a shows the STEM-EELS probe positions overlapping the simultaneously acquired ADF-STEM image. The probe positions are colored based on the dimensionality reduction and clustering results. The visualization of the data clustering via NMF, t-SNE, and GMM is shown in Figure 4b. The probe locations of all the EELS spectra from four clusters can be directly visualized in Figure 4a, and each cluster mostly corresponds to a single region on the stacked J14 thin film. The analysis successfully categorized the EELS spectra from MgO (green), 500°C J14 thin film (navy), 200°C J14 thin film (red), and carbon deposition (cyan), and the class-averaged O k edge ELNES from each cluster are plotted with corresponding colors in Figure 4c-f. When comparing the spectra representing two parts of the thin films, the most significant difference is the emergence of the peak at around 529 eV, related to the unoccupied 3d states.[31] The emergence of the peak indicates a drastic change in the configurations in the 3d orbitals for the transition metal cations.

To pinpoint the origin of the 3d orbital changes, we acquired the core loss line-scan EELS data of the transition metal L edges (Figure 5). The probe positions overlapped on the ADF-STEM

image are plotted in Figure 5a. The ELNES for Co, Ni, and Cu L edges are plotted in Figure 5b-d, respectively, with the colors matching the color of the probe positions in Figure 5a. In Figure 5b, significant variations of spectral features, such as the edge onset energy and shapes, are evident in the Co L edges ELNES across the stacked thin film. The difference in ELNES highlights the change of 3d orbital configurations and chemical environment for Co ions. On the other hand, the L edges ELNES of Ni, Cu, and Zn do not exhibit noticeable changes (Figure S2). To closely examine the chemical environment for the Co ions, the averaged ELNES for Co L edges from 200°C and 500°C J14, as well as the reference spectra from CoO and Co_3O_4, are plotted in Figure 5e.[32] The ELNES collected from the 500°C J14 resembles the reference spectra from CoO, which is expected since the J14 ESO crystalizes in the rocksalt form with the constituent cations having the 2+ oxidation states. However, the ELNES collected from 200°C J14 show remarkable similarity to the Co_3O_4 reference spectra. This similarity implies the Co oxidation states change from 2+ to 3+ and a bonding environment change. We also calculated the intensity ratio of the L_3 and L_2 peaks for Co across the stacked thin film and mapped the ratio in Figure S3. Since the intensity ratio of the white lines is closely related to the unoccupied states in 3d levels, EELS can be used to determine the oxidation states in the transitional metal.[33] The averaged L_3/L_2 ratio is approximately 3.3 and 4.3, corresponding to the oxidation states of 2.6+ and 2.1+ for the 200°C J14 and 500°C J14, respectively.[33] The Co oxidation states in 200°C J14 roughly match those in the Co_3O_4 with spinel structure.

The Co chemical environment shift measured with STEM-EELS correlates with the out-of-plane lattice parameter change in the stacked thin-film quantified by 4D-STEM. Firstly, The ionic radius for low spin Co^{3+} shrinks by around 27% compared to the high spin Co^{2+} based on the Shannon ionic radii.[34] Second, the Co ions in 200°C J14 have a similar bonding environment to the spinel

Co_3O_4, which has a similar oxygen lattice structure to CoO but a 5% smaller O^{2-} distance.[35] Combining the abovementioned factors, we hypothesize that the reduction of the lattice parameter is due to the Co chemical environment shift. We further hypothesize the potential reason for the Co chemical environment change could be correlated with the higher level of cation vacancies in 200°C J14, since the low substrate temperature results in a more oxidative condition at the growth surface and leads to the formation of Co^{3+} and cation vacancies for charge neutrality.[36,37]

First principle density functional theory (DFT) calculations were employed on special quasi-random structures (SQSs) of J14 to investigate this hypothesis.[38] A pristine rocksalt J14 SQS ($J14_{pris}$) and a rocksalt J14 SQS with point defects on the cation sublattice ($J14_{vac}$) were used to model the high (500°C) and low (200°C) temperature J14 films, respectively. The percentage of vacancies (6.25%) was approximated based on charge neutrality conditions from the average cobalt valence from EELS fitting. The fully relaxed bulk lattice parameter of the pristine J14 512-atom SQS was found to be 4.2102 Å, in agreement with previous extended x-ray absorption fine structure (EXAFS) reports on bulk J14 [16](4.230 ± 0.005 Å). A -0.5% in-plane strain (ε_{xx}) was enforced on further calculations to mimic the epitaxially strained nature of the HEO films, while the out-of-plane cell vector and atoms were under no constraints during relaxation. Based on the similarity of EELS of the 200°C film to the spinel Co_3O_4 with octahedrally coordinated low-spin Co^{3+}, the cobalt ions were initialized in a low-spin state for the $J14_{vac}$ calculation. An additional calculation with cobalt ions initialized in a high-spin state is shown in Figure S4 for completeness.

The out-of-plane strains (ε_{yy}) for the relaxed structures were calculated as +1.71% and -0.77% for $J14_{pris}$ and $J14_{vac}$ relative to the enforced ε_{xx} (Figures 6a and 6b), in qualitative agreement with the 4D-STEM strain measurement results. Co Bader charge in $J14_{pris}$ was centered around 1.23 (Figure 6c), while a large fraction of the Co atoms in $J14_{vac}$ showed an increased Bader charge

(Figure 6d). Two distributions of increased Bader charge in $J14_{vac}$ can be seen centered around approximately 1.32 and 1.38. A smaller fraction of the Ni and Cu ions within the $J14_{vac}$ SQS also showed an increased Bader charge, while no changes were observed for Mg or Zn. The ratio of cations identified as 2+ and 3+ within the $J14_{vac}$ SQS are summarized in Figure 6e. 44% of the Co ions were identified in a 3+ valence in the $J14_{vac}$ SQS, while only 10% and 12% were found for Ni and Cu, respectively, suggesting that the charge compensation of cation vacancies in the J14 rocksalt matrix occurs primarily through the oxidation of Co^{2+} to Co^{3+}. Overall, the DFT calculations show that vacancies on the cation sublattice of J14 result in significant changes both electronically and structurally within the rocksalt HEO matrix.

CONCLUSION

In summary, we have investigated the nanostructures and chemical environment in the stacked J14 HEO thin film synthesized using PLD at 200°C and 500°C. STEM-EDX elemental mapping indicated the cation deficiency in the 200°C J14 film compared to the 500°C film. SAED pattern showed no evidence of a secondary phase but indicated varied out-of-plane lattice parameters within the stacked film. The atomically resolved ADF-STEM images revealed a larger lattice parameter in 500°C J14 compared to the 200°C J14. With 4D-STEM strain measurement, we have quantified the out-of-plane lattice parameter difference to be +1% and -1% for 500°C and 200°C J14 films, respectively, compared to the MgO substrate. Monochromated STEM-EELS resolved the energy loss near edge structure for the constituent elements, and a drastic change in chemical environment for Co and O was discovered across the stacked film, whereas for other elements, it remained constant. The Co changed its oxidation states from Co^{2+} to Co^{3+} (smaller ionic radius) in 200°C J14 film, and its bonding environment was akin to that in Co_3O_4. DFT calculations show that the generation of the Co^{3+} in 200°C J14 is linked to charge compensation of the cation vacancies, which leads a reduction of the lattice parameter. Consequently, our combined

experimental and theory results show that the variations in the structural, optical and magnetic properties[18] in the film grown at lower substrate temperatures can be directly linked to the chemical environment change for Co due to cation deficiency. Our results indicate that the nanostructure and chemical environment in the HEO thin films are heavily impacted by a complex correlation between configurational entropy, thermodynamics, and kinetics during the PLD growth process.[22,39] In addition to the compositional variations and substrate temperature, it has been previously shown that PLD can control the structures and properties of numerous oxide thin films via controlling other growth conditions such as oxygen partial pressure and laser beam profiles.[19,40–42] We believe there are undoubtedly many more possible nanostructures within the vast configurational space in HEO that can be accessed via tailoring the specific kinetic parameters during the synthesis. Tuning these growth parameters during synthesis would pave the path for engineering novel nanostructures for functional properties in HEO materials.
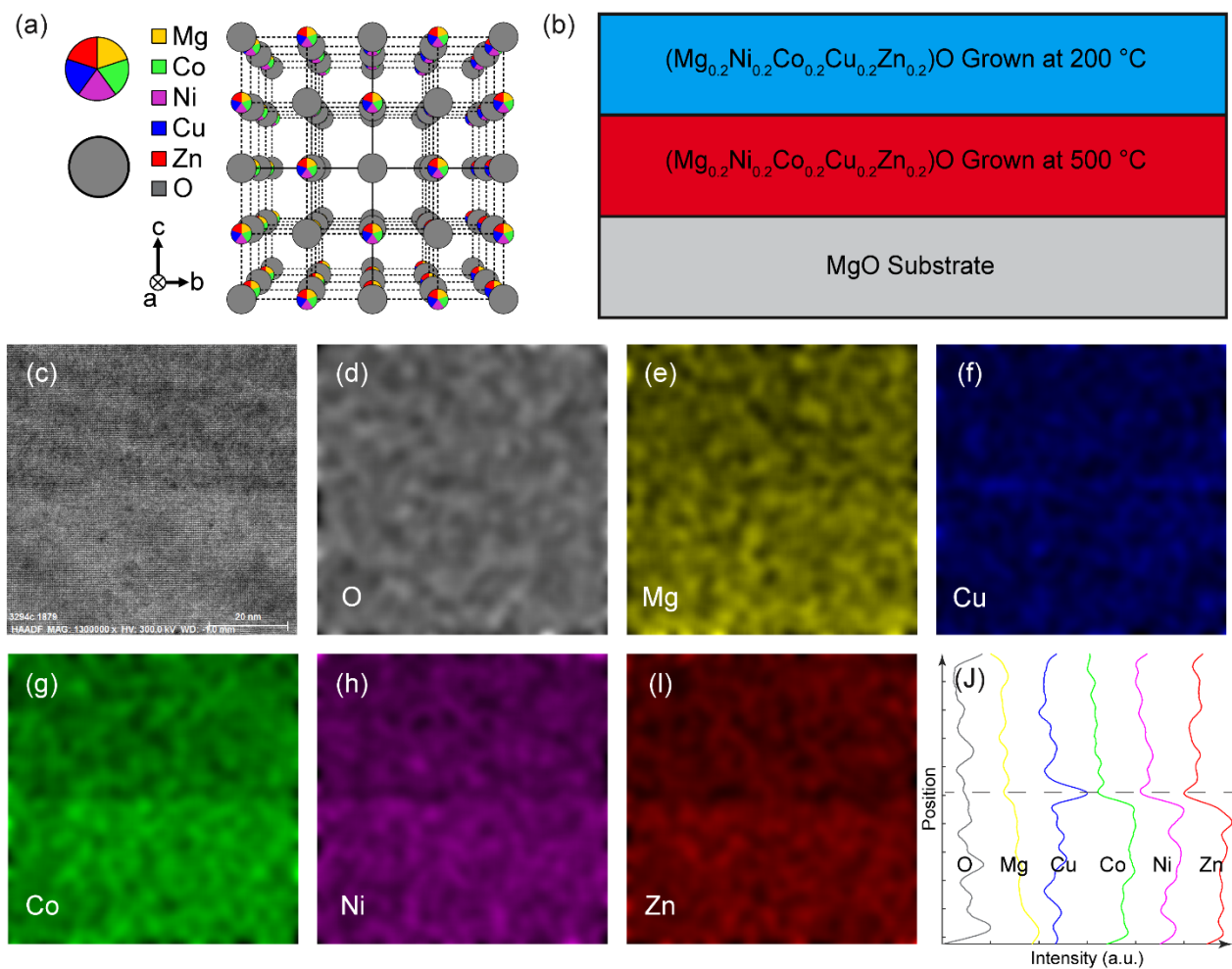
Figure 1. (a) The crystal structure model for the rocksalt structure HEO (Mg$_{0.2}$, Co$_{0.2}$, Ni$_{0.2}$, Cu$_{0.2}$, Zn$_{0.2}$) O viewing from the [100] axis; (b) the schematics of the stacked HEO thin film synthesized with PLD method. (c) the high-resolution HAADF-STEM micrograph acquired at the interface of the stacked thin film and (d-l) the EDX map of the constituent elements taken at the same region as the HAADF-STEM micrograph in (c). (J) the line averaged EDX intensity profile with the interface location marked by the dashed line.
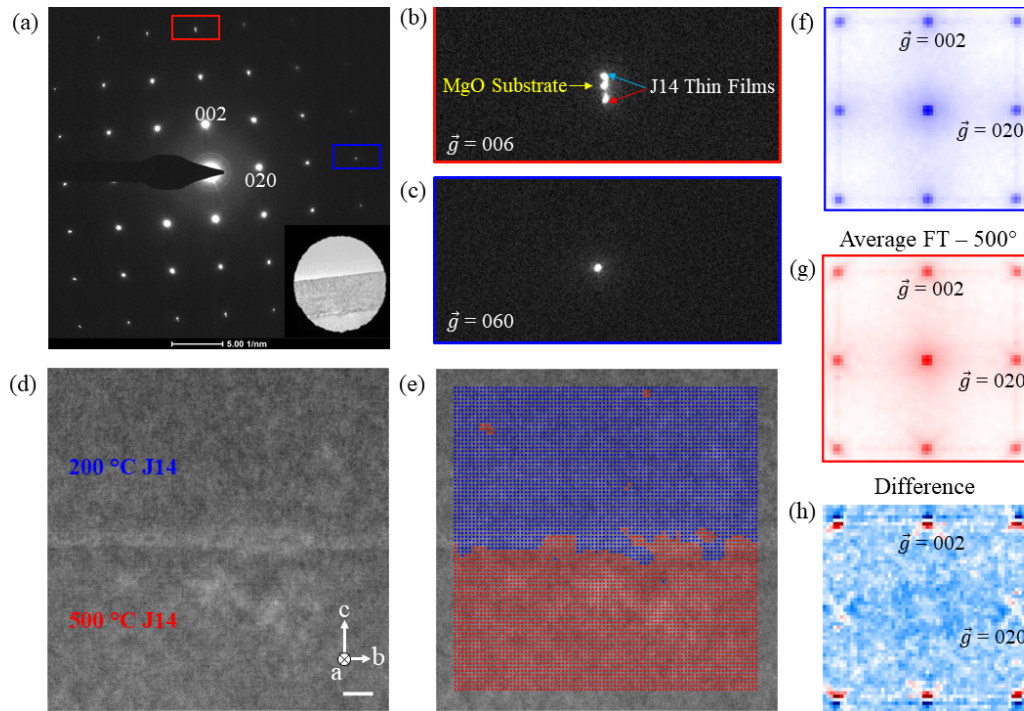
Figure 2. The reciprocal space investigation and the local crystallography analysis. (a) the SAED pattern acquired from the stacked HEO thin film from the [100] zone axis. Inset: location of the selected area diffraction aperture. (b) the magnified image of the split g = 006 reflections and (c) the magnified image of the sharp g = 060 reflections; (b) and (c) are cropped from the red and blue boxes in (a), respectively. (d) atomically resolved HAADF-STEM image taken at the stacked film interface between 200°C J14 and 500°C J14. (e) the result of the image segmentation on the same HAADF-STEM image using the physics-based deep learning analysis on the local crystallographic information. The spots represent the center positions of the window where the local FT patterns were extracted. The local FT patterns were categorized into two classes via analyzing the local crystallographic information. The spots were colored based on the categorization results. (f) and (g) the class-averaged FT pattern from two classes primarily found in 200°C J14 and 500°C J14 film, respectively. (h) the difference between the class averaged FT patterns in (f) and (g).
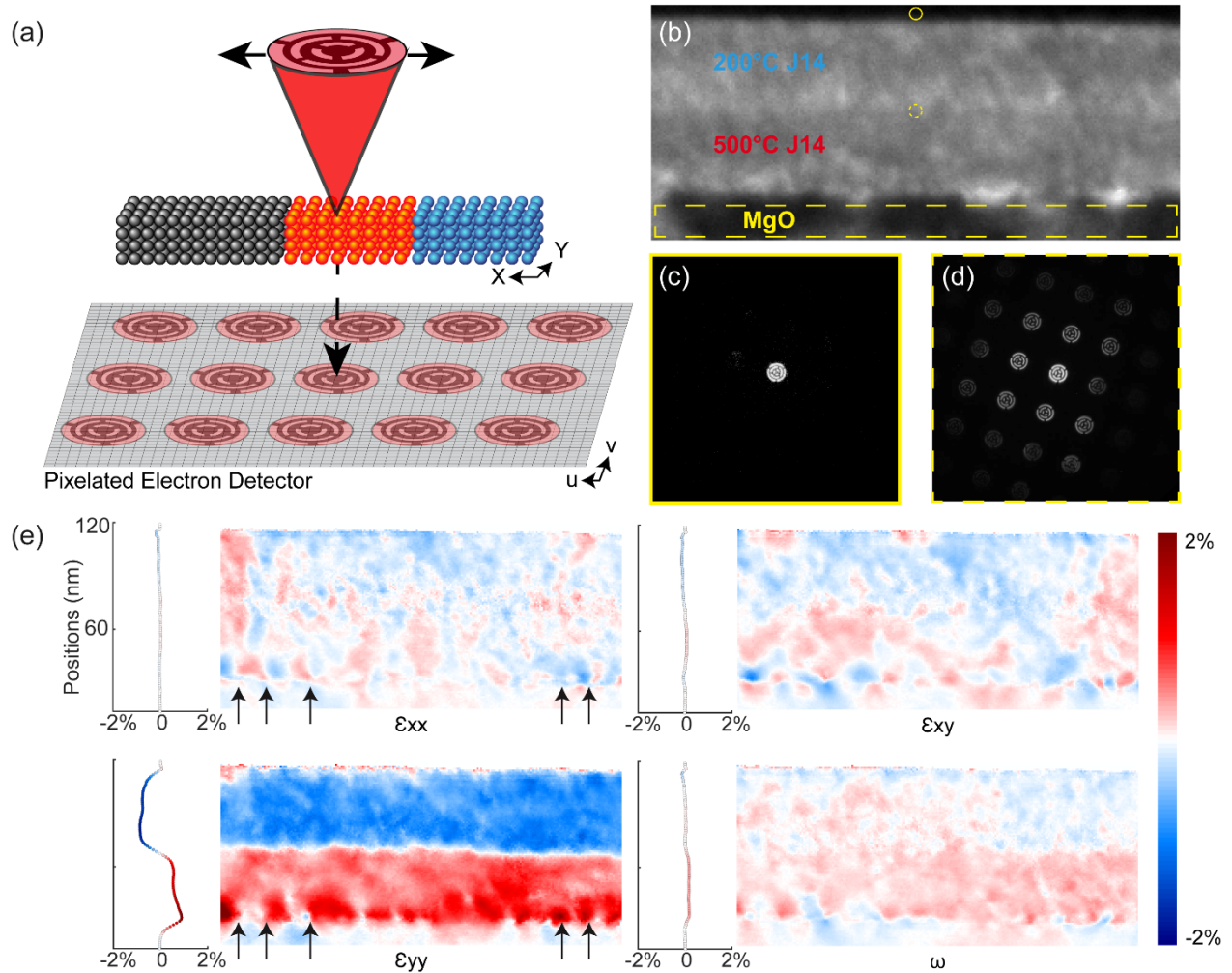
Figure 3. The four-dimensional STEM (4D-STEM) results in the stacked HEO thin film. (a) the schematics of the 4D-STEM experimental setup using the patterned condenser aperture. (b) the virtual ADF-STEM image generated from the 4D-STEM dataset and (c-d) the examples of the nanobeam electron diffraction (NBED) patterns within the 4D-STEM dataset. The NBED patterns were acquired at (c) the carbon deposition and (d) the stacked film, and the corresponding probe positions were marked with pink and green dots in (b); (e) the strain mapping of in-plane (εxx), shear (εxy), out-of-plane (εyy), and rotation components (ω) measured from the 4D-STEM dataset. The line average strain profiles are plotted on the side. The reference region on the MgO substrate is marked with a yellow dashed box in (b).
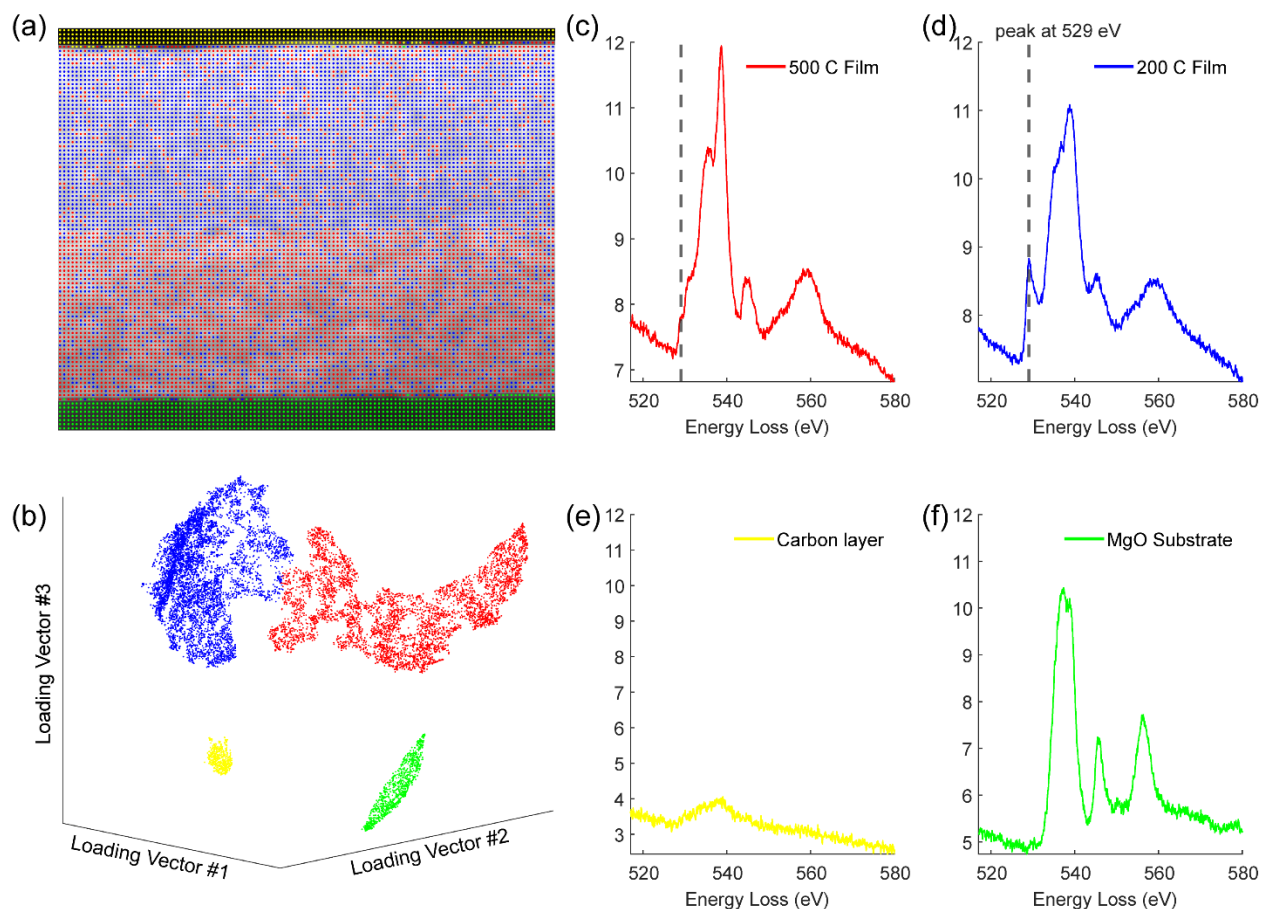
Figure 4. The unsupervised machine learning analysis of the STEM-EELS for oxygen K edge. (a) the probe positions overlaid over the ADF-STEM image. The probe positions are categorized into four classes and colored based on the clustering results in (b) the visualization of the gaussian mixture model (GMM) clustering results after the dimensionality reduction using non-negative matrix factorization and t-distributed stochastic neighbor embedding (t-SNE). (c-f) the class-averaged EELS spectra for four classes are primarily found in 500°C J14 film, 200°C J14 film, carbon layer, and MgO substrate. The dashed line in (d) marks the position of the extra peak compared to (c).
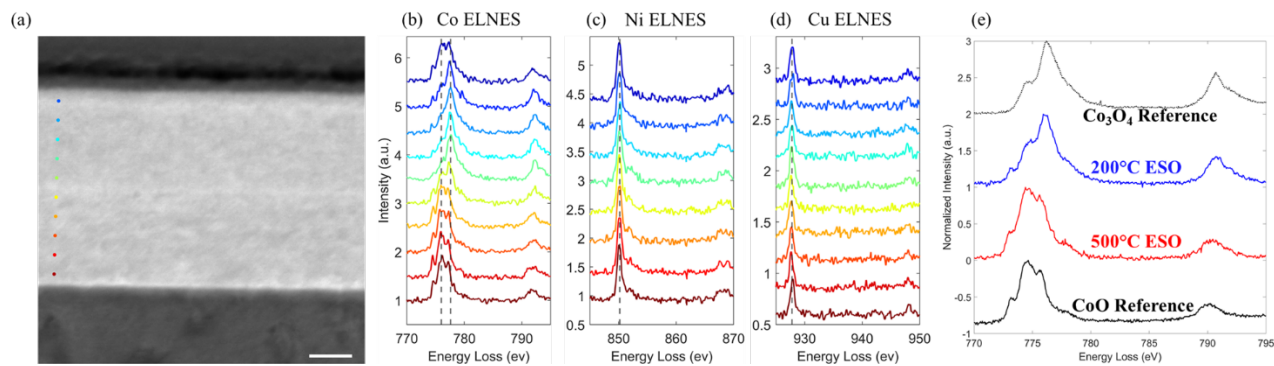
Figure 5. The line-scan monochromated STEM-EELS of 3d transition metal L edge energy loss near edge structure (ELNES). (a) the probe positions overlaid over the ADF-STEM image. (b-d) The L edge ELNES for Co, Ni, and Cu, respectively. (e) The comparison between the averaged spectra from 200°C J14 film, 500°C J14 film, CoO reference spectra, and Co_3O_4 reference spectra.
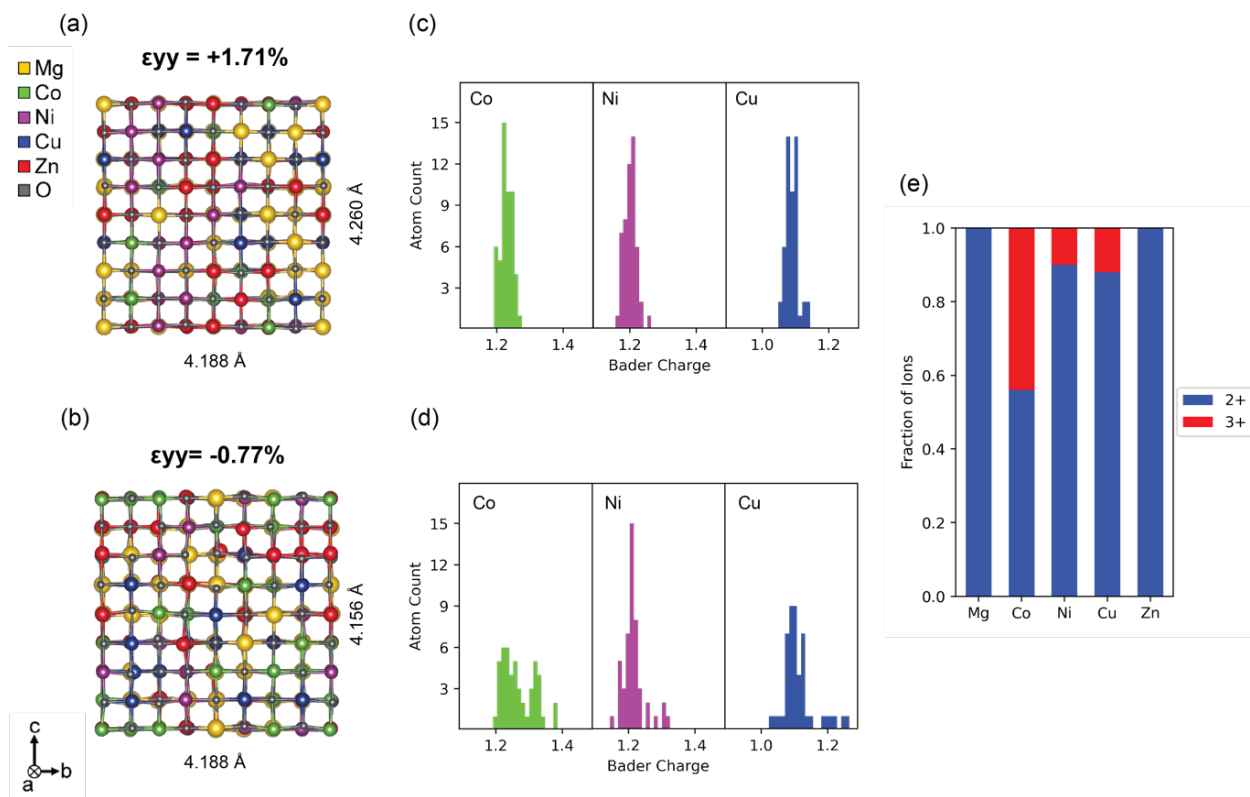
Figure 6. Results from DFT calculations of the pristine (J14$_{pris}$) and defect (J14$_{vac}$) SQSs corresponding to the high (500°C) and low (200°C) temperature films, respectively. Relaxed structures for J14$_{pris}$ and J14$_{vac}$ with corresponding lattice parameters and out-of-plane strain (ε_{yy}) values are shown in (a) and (b), respectively. Bader charge distributions for J14$_{pris}$ (c) and J14$_{vac}$ (d) predict a significant change in cobalt valence state when vacancies on the cation sublattice are present. The relative amount of 2+ and 3+ cations within the J14$_{vac}$ SQS is summarized in (e). Visualization was performed with VESTA.[43]

ASSOCIATED CONTENT

The Supporting Information is available free of charge at

https://pubs.acs.org/doi/(will be provided by publisher)

Supporting Information: unsupervised machine learning algorithm flow chart, STEM-EELS data for Co, Ni, Cu and Zn, and STEM-EELS L_3/L_2 ratio calculations and valence mapping. (PDF)

AUTHOR INFORMATION

Corresponding Author

*Nasim Alem

Email: nua10@psu.edu

Author Contributions

L.M. and N.A. designed the study and performed the electron microscopy experiments and analysis. J.T.S, I.D. and S.B.S carried out the density functional theory calculations. G.N.K and J-P.M envisioned and synthesized the HEO thin film. J.C. and C.O. performed 4D-STEM and EELS at the Molecular Foundry. The manuscript was written through contributions of all authors. All authors have given approval to the final version of the manuscript.

METHODS

Pulsed Laser Deposition (PLD). The stacked $Mg_{0.2}Ni_{0.2}Co_{0.2}Cu_{0.2}Zn_{0.2}O$ epitaxial thin film was grown using PLD and conditions reported previously.[18] A single phase ceramic ablation target was reactively sintered using a stoichiometric mixture of binary oxide powders: MgO ($\geq$99%), CoO

($\geq$99%), NiO (99.99%), CuO (99.99%), and ZnO (99.999%). The mixture was pressed uniaxially, then isostatically, then sintered at 1000°C for 12 hours and air-quenched to obtain a single rocksalt phase. The thin film was grown on a [100] MgO substrate in 50 mTorr of flowing oxygen, with a laser pulse rate of 6 Hz and a laser fluence of 1.2 J/cm^2 using a Coherent 248 nm KrF laser. The substrate temperature was initially set to 500 °C for growth of the first, underlying epitaxial layer. The substrate was promptly cooled to 200 °C (< 15 minutes time elapsed), and a second layer was deposited directly on top. All other growth conditions remained constant. The stacked film was then quenched to ambient lab temperature (~25 °C) within 2 minutes of the last laser pulse.

Transmission electron microscopy (TEM). The cross-sectional TEM samples were extracted using the standard focused ion beam (FIB) preparation method. The FIB lamella was thinned down with 30kV and 5kV ion beam followed by the final cleaning with 2kV and 1kV ion beam. The selected area electron diffraction (SAED) patterns were collected with ThermoFisher Talos 200X S/TEM operating at 200 kV. The scanning transmission electron microscopy (STEM) was performed using ThermoFisher Titan G2 S/TEM equipped with the probe corrector operating at 300kV. The annular dark field (ADF-) STEM was performed with the convergence angle of 30 mrad and collection angle of 44-200 mrad. The dwell time during the acquisition for ADF-STEM image is 2 μs. Each STEM dataset contains two consecutively acquired images with perpendicular scanning directions for the post-acquisition drift correction.[44]

Four-dimensional STEM (4D-STEM). The 4D-STEM data was collected using the TEAM I S/TEM at the National Center for Electron Microscopy (NCEM). The acceleration voltage was 80 kV for avoiding the electron beam damage. The 4D-STEM data was collected with the Gatan K3 direct electron detector. The patterned condenser aperture with the convergence angle of 4 mrad was used for increasing the precision of the strain quantification. The dwell time for each

nanobeam electron diffraction (NBED) pattern is 0.02 seconds, and the angle range for the NBED patterns are 0-60.3 mrad. In real space, the scanning size is 224 pixels by 103 pixels and the step size is 1.03 nm. The total acquisition time is 7 minutes and 47 seconds.

The 4D-STEM data processing was performed using the py4DSTEM[45] package in python. The strain measurement was done by measuring the diffracted disk position in each NBED using a template matching algorithm. One 4D-STEM dataset was acquired from the same session in the vacuum region to generate the probe template. The original data set has a dimension of 1024 by 1024 pixels for each NBED pattern, and it is downsized to 512 by 512 pixels to increase the processing speed.

Electron energy loss spectroscopy (EELS). All EELS data was acquired in STEM-EELS mode to spatially resolve the chemical environment information. The acceleration voltage was 80 kV for reducing the beam damage during the acquisition. The EELS mapping were acquired using the Gatan K3 detector in TEAM I S/TEM at NCEM with monochromator activated (energy resolution of 0.25 eV). The data was collected during the same session as the 4D-STEM experiment on roughly the same region. The acquisition time per pixel was 0.025 seconds with sub-pixel scanning enabled. The convergence was 8 mrad and the collection angle is 100 mrad.

The transition metal L edge energy loss near edge structure data (ELNES) were acquired with ThermoFisher Titan G2 S/TEM with monochromator activated (energy resolution of 0.18 eV) at Penn State. The ELNES data was collected in the line-scan mode with the acquisition time per probe position was 0.5-2 seconds. The 2.5mm entrance aperture was used and the collection angle was 12.2 mrad. The noise in the L edge ELNES data is reduced with the principal component analysis (PCA) method by selecting the first 5 components.

Unsupervised Machine Learning. The unsupervised machine learning algorithm for the STEM image processing, similar to the analysis in the previous report[23], is performed using the in-house developed MATLAB scripts. The flowchart of is shown in Figure S1. The input STEM image was cropped with a sliding window and forming a stack of sub-images with the dimension of (h by w by n). In this work, the height (h) and width (w) of the window is 200 pixels, the step size for each window position is 20 pixels, and the resulting stack has 6724 (n) sub-images. The two-dimensional Fourier transformation (FT) was performed on each sub-image in the stack to reflect the local periodicity within each window, and the three-dimensional stack was flattened into two-dimension of h·w by n. The dimensionality reduction with principal component analysis (PCA) and clustering with gaussian mixture model (GMM) are performed on the data. The first two principal components were used for the GMM clustering. The FT patterns were categorized into two classes marked with red and blue spots. The center of the cropping window is colored according to the clustering results and mapped on the original image to specify the class of each window. The class-averaged FT patterns and the difference from each class are then calculated.

The unsupervised machine learning algorithm for the STEM-EELS analysis, similar to the previous report[30], is performed using the in-house developed MATLAB scripts. The STEM-EELS data is originally a three-dimensional spectral image (h by w by n channels), and it is firstly flattened into two dimensions (h·w by n). The dimensionality reduction with non-negative matrix factorization (NMF) was performed on flattened data, and the dimensionality was reduced to three loading vectors and the corresponding scores for the loading vectors. Subsequently, the t-distributed stochastic neighbor embedding (t-SNE) was applied on the NMF loading vectors and coefficient. It has been demonstrated that the combination of NMF and t-SNE would result in more distinguishable fine structures in the spectra. The gaussian mixture model (GMM) was used for

data clustering into four classes. The probe position is plotted over the ADF-STEM image and colored according to the classes to indicate the spatial positions of each class. The class-averaged EELS data was extracted based on the clustering result to visualize the spectral differences.

Computational Methods. DFT calculations were performed with the Vienna *Ab-initio* Simulation Package (VASP) 5.4.1 with the PBEsol functional.[46,47] The valence electrons considered within the calculations are $2p^63s^2$ for Mg, $3d^74s^2$ for Co, $3p^63d^94s^1$ for Ni, $3p^63d^{10}4s^1$ for Cu, $3d^{10}4s^2$ for Zn, and $2s^22p^4$ for O using the standard PAW potentials. DFT+U was used to more properly describe the localized *d*-electrons of Co, Ni, and Cu within the simplified (rotational invariant) approach with U values of 4, 5, and 5 eV, respectively, based on ancillary sensitivity tests for the binary rocksalt oxides.[48] A plane wave cutoff of 600 eV was used for all calculations. Only the Γ-point was used to sample the Brillouin zone with a Gaussian smearing of 0.05 eV. The magnetic ions (Co, Ni, Cu) were initialized with an antiferromagnetic (AFM) ordering with alternating ferromagnetic planes parallel to the (111) direction as found previously for J14.[49] 4x4x4 supercells of the rocksalt unit cell were used for all calculations. Convergence was assumed when the energy difference between two consecutive self-consistent cycles was less than 10^{-6} eV with forces relaxed until they were less than 10 meV/Å. Bader charge analysis was performed using the software from the Henkelman group[50] and SQS generation was performed using the integrated cluster expansion toolkit (ICET).[51] An additional calculation of the J14vac SQS was performed to sample other possible spin-states of Co3+, where Co was initialized in the high-spin state. This is summarized in Figure S4. A similar amount of Co3+ ions resulted with a smaller change in εyy compared to the J14vac calculation within the main text. This is expected as the Shannon ionic radius of high-spin Co3+ is larger than that of the low-spin Co3+.[34]

ACKNOWLEDGMENT

REFERENCES

(1)   Sarkar, A.; Breitung, B.; Hahn, H. High Entropy Oxides: The Role of Entropy, Enthalpy and Synergy. *Scr. Mater.* **2020**, *187*, 43–48. https://doi.org/10.1016/j.scriptamat.2020.05.019.

(2)   Cantor, B.; Chang, I. T. H.; Knight, P.; Vincent, A. J. B. Microstructural Development in Equiatomic Multicomponent Alloys. *Mater. Sci. Eng. A* **2004**, *375–377* (1-2 SPEC. ISS.), 213–218. https://doi.org/10.1016/j.msea.2003.10.257.

(3)   Yeh, J. W.; Chen, S. K.; Lin, S. J.; Gan, J. Y.; Chin, T. S.; Shun, T. T.; Tsau, C. H.; Chang, S. Y. Nanostructured High-Entropy Alloys with Multiple Principal Elements: Novel Alloy

Design Concepts and Outcomes. *Adv. Eng. Mater.* **2004**, *6* (5), 299–303. https://doi.org/10.1002/adem.200300567.

(4)   Rost, C. M.; Sachet, E.; Borman, T.; Moballegh, A.; Dickey, E. C.; Hou, D.; Jones, J. L.; Curtarolo, S.; Maria, J. P. Entropy-Stabilized Oxides. *Nat. Commun.* **2015**, *6* (1), 1–8. https://doi.org/10.1038/ncomms9485.

(5)   Dąbrowa, J.; Stygar, M.; Mikuła, A.; Knapik, A.; Mroczka, K.; Tejchman, W.; Danielewski, M.; Martin, M. Synthesis and Microstructure of the (Co,Cr,Fe,Mn,Ni)3O4 High Entropy Oxide Characterized by Spinel Structure. *Mater. Lett.* **2018**, *216*, 32–36. https://doi.org/10.1016/j.matlet.2017.12.148.

(6)   Jiang, S.; Hu, T.; Gild, J.; Zhou, N.; Nie, J.; Qin, M.; Harrington, T.; Vecchio, K.; Luo, J. A New Class of High-Entropy Perovskite Oxides. *Scr. Mater.* **2018**, *142*, 116–120. https://doi.org/10.1016/j.scriptamat.2017.08.040.

(7)   Chen, K.; Pei, X.; Tang, L.; Cheng, H.; Li, Z.; Li, C.; Zhang, X.; An, L. A Five-Component Entropy-Stabilized Fluorite Oxide. *J. Eur. Ceram. Soc.* **2018**, *38* (11), 4161–4164. https://doi.org/10.1016/j.jeurceramsoc.2018.04.063.

(8)   Zhou, J.; Zhang, J.; Zhang, F.; Niu, B.; Lei, L.; Wang, W. High-Entropy Carbide: A Novel Class of Multicomponent Ceramics. *Ceram. Int.* **2018**, *44* (17), 22014–22018. https://doi.org/10.1016/j.ceramint.2018.08.100.

(9)   Moskovskikh, D.; Vorotilo, S.; Buinevich, V.; Sedegov, A.; Kuskov, K.; Khort, A.; Shuck, C.; Zhukovskyi, M.; Mukasyan, A. Extremely Hard and Tough High Entropy Nitride Ceramics. *Sci. Rep.* **2020**, *10* (1), 1–8. https://doi.org/10.1038/s41598-020-76945-y.

(10)   Jiang, B.; Yu, Y.; Cui, J.; Liu, X.; Xie, L.; Liao, J.; Zhang, Q.; Huang, Y.; Ning, S.; Jia, B.; Zhu, B.; Bai, S.; Chen, L.; Pennycook, S. J.; He, J. High-Entropy-Stabilized Chalcogenides with High Thermoelectric Performance. *Science* **2021**, *371* (6531), 830–834. https://doi.org/10.1126/science.abe1292.

(11)   Sarkar, A.; Velasco, L.; Wang, D.; Wang, Q.; Talasila, G.; de Biasi, L.; Kübel, C.; Brezesinski, T.; Bhattacharya, S. S.; Hahn, H.; Breitung, B. High Entropy Oxides for Reversible Energy Storage. *Nat. Commun.* **2018**, *9* (1), 1–9. https://doi.org/10.1038/s41467-018-05774-5.

(12)   Bérardan, D.; Franger, S.; Meena, A. K.; Dragoe, N. Room Temperature Lithium Superionic Conductivity in High Entropy Oxides. *J. Mater. Chem. A* **2016**, *4* (24), 9536–9541. https://doi.org/10.1039/c6ta03249d.

(13)   Qiu, N.; Chen, H.; Yang, Z.; Sun, S.; Wang, Y.; Cui, Y. A High Entropy Oxide (Mg0.2Co0.2Ni0.2Cu0.2Zn0.2O) with Superior Lithium Storage Performance. *J. Alloys Compd.* **2019**, *777*, 767–774. https://doi.org/10.1016/j.jallcom.2018.11.049.

(14)   Cavin, J.; Ahmadiparidari, A.; Majidi, L.; Thind, A. S.; Misal, S. N.; Prajapati, A.; Hemmat, Z.; Rastegar, S.; Beukelman, A.; Singh, M. R.; Unocic, K. A.; Salehi-Khojin, A.; Mishra, R. 2D High-Entropy Transition Metal Dichalcogenides for Carbon Dioxide Electrocatalysis. *Adv. Mater.* **2021**, *33* (31), 2100347. https://doi.org/10.1002/adma.202100347.

(15)   Moździerz, M.; Dąbrowa, J.; Stępień, A.; Zajusz, M.; Stygar, M.; Zając, W.; Danielewski, M.; Świerczek, K. Mixed Ionic-Electronic Transport in the High-Entropy (Co,Cu,Mg,Ni,Zn)1-XLixO Oxides. *Acta Mater.* **2021**, *208*, 116735.

https://doi.org/https://doi.org/10.1016/j.actamat.2021.116735.

(16) Rost, C. M.; Rak, Z.; Brenner, D. W.; Maria, J. P. Local Structure of the MgxNixCoxCuxZnxO(X=0.2) Entropy-Stabilized Oxide: An EXAFS Study. *J. Am. Ceram. Soc.* **2017**, *100* (6), 2732–2738. https://doi.org/10.1111/jace.14756.

(17) Dupuy, A. D.; Wang, X.; Schoenung, J. M. Entropic Phase Transformation in Nanocrystalline High Entropy Oxides. *Mater. Res. Lett.* **2019**, *7* (2), 60–67. https://doi.org/10.1080/21663831.2018.1554605.

(18) Kotsonis, G. N.; Meisenheimer, P. B.; Miao, L.; Roth, J.; Wang, B.; Shafer, P.; Engel-Herbert, R.; Alem, N.; Heron, J. T.; Rost, C. M.; Maria, J. P. Property and Cation Valence Engineering in Entropy-Stabilized Oxide Thin Films. *Phys. Rev. Mater.* **2020**, *4* (10), 1–9. https://doi.org/10.1103/PhysRevMaterials.4.100401.

(19) Kotsonis, G. N.; Rost, C. M.; Harris, D. T.; Maria, J. P. Epitaxial Entropy-Stabilized Oxides: Growth of Chemically Diverse Phases via Kinetic Bombardment. *MRS Commun.* **2018**, *8* (3), 1371–1377. https://doi.org/10.1557/mrc.2018.184.

(20) Miao, L.; Kotsonis, G.; Ciston, J.; Ophus, C.; Maria, J.-P.; Alem, N. Impact of the Synthesis Kinetics of Entropy-Stabilized Oxide Thin Films Probed with 4D-STEM and STEM-EELS. *Microsc. Microanal.* **2021**, *27* (S1), 352–354. https://doi.org/10.1017/S143192762100180X.

(21) Kotsonis, G. N. High-Entropy Oxides: Epitaxial Growth, Kinetic Dependencies, and Linear Optical Properties, The Pennsylvania State University, 2022.

(22) Rost, C. M. Entropy-Stabilized Oxides: Explorations of a Novel Class of Multicomponent

Materials-PhD Thesis,. *North Carolina State Univ.* **2016**, 227.

(23)   Vasudevan, R. K.; Ziatdinov, M.; Jesse, S.; Kalinin, S. V. Phases and Interfaces from Real Space Atomically Resolved Data: Physics-Based Deep Data Image Analysis. *Nano Lett.* **2016**, *16* (9), 5574–5581. https://doi.org/10.1021/acs.nanolett.6b02130.

(24)   Somnath, S.; Smith, C. R.; Kalinin, S. V.; Chi, M.; Borisevich, A.; Cross, N.; Duscher, G.; Jesse, S. Feature Extraction via Similarity Search: Application to Atom Finding and Denoising in Electron and Scanning Probe Microscopy Imaging. *Adv. Struct. Chem. Imaging* **2018**, *4* (1), 1–10. https://doi.org/10.1186/s40679-018-0052-y.

(25)   Zeltmann, S. E.; Müller, A.; Bustillo, K. C.; Savitzky, B.; Hughes, L.; Minor, A. M.; Ophus, C. Patterned Probes for High Precision 4D-STEM Bragg Measurements. *Ultramicroscopy* **2020**, *209*, 112890. https://doi.org/10.1016/j.ultramic.2019.112890.

(26)   Lucas, G.; Burdet, P.; Cantoni, M.; Hébert, C. Multivariate Statistical Analysis as a Tool for the Segmentation of 3D Spectral Data. *Micron* **2013**, *52–53*, 49–56. https://doi.org/https://doi.org/10.1016/j.micron.2013.08.005.

(27)   Nicoletti, O.; de la Peña, F.; Leary, R. K.; Holland, D. J.; Ducati, C.; Midgley, P. A. Three-Dimensional Imaging of Localized Surface Plasmon Resonances of Metal Nanoparticles. *Nature* **2013**, *502* (7469), 80–84. https://doi.org/10.1038/nature12469.

(28)   Shiga, M.; Tatsumi, K.; Muto, S.; Tsuda, K.; Yamamoto, Y.; Mori, T.; Tanji, T. Sparse Modeling of EELS and EDX Spectral Imaging Data by Nonnegative Matrix Factorization. *Ultramicroscopy* **2016**, *170*, 43–59. https://doi.org/https://doi.org/10.1016/j.ultramic.2016.08.006.

(29)   Dobigeon, N.; Brun, N. Spectral Mixture Analysis of EELS Spectrum-Images. *Ultramicroscopy* **2012**, *120*, 25–34. https://doi.org/10.1016/j.ultramic.2012.05.006.

(30)   Ryu, J.; Kim, H.; Myeong, R.; Kim, S.; Jo, J.; Lee, S.; Tae, K.; Joo, Y.; Yi, G.; Lee, J.; Kim, M. Ultramicroscopy Dimensionality Reduction and Unsupervised Clustering for EELS-SI. *Ultramicroscopy* **2021**, No. May, 113314. https://doi.org/10.1016/j.ultramic.2021.113314.

(31)   Frati, F.; Hunault, M. O. J. Y.; De Groot, F. M. F. Oxygen K-Edge X-Ray Absorption Spectra. *Chem. Rev.* **2020**, *120* (9), 4056–4110. https://doi.org/10.1021/acs.chemrev.9b00439.

(32)   Ewels, P.; Sikora, T.; Serin, V.; Ewels, C. P.; Lajaunie, L. A Complete Overhaul of the Electron Energy-Loss Spectroscopy and X-Ray Absorption Spectroscopy Database: Eelsdb.Eu. *Microsc. Microanal.* **2016**, *22* (3), 717–724. https://doi.org/10.1017/S1431927616000179.

(33)   Wang, Z. L.; Yin, J. S.; Jiang, Y. D. EELS Analysis of Cation Valence States and Oxygen Vacancies in Magnetic Oxides. *Micron* **2000**, *31* (5), 571–580. https://doi.org/10.1016/S0968-4328(99)00139-0.

(34)   Shannon, R. D. Revised Effective Ionic Radii and Systematic Studies of Interatomic Distances in Halides and Chalcogenides. *Acta Crystallogr. Sect. A* **1976**, *32* (5), 751–767. https://doi.org/10.1107/S0567739476001551.

(35)   Carson, G. A.; Nassir, M. H.; Langell, M. A. Epitaxial Growth of Co3O4 on CoO(100). *J. Vac. Sci. Technol. A* **1996**, *14* (3), 1637–1642. https://doi.org/10.1116/1.580310.

(36)   Chen, M.; Hallstedt, B.; Gauckler, L. J. Thermodynamic Assessment of the Co-O System.

J. Phase Equilibria **2003**, *24* (3), 212–227. https://doi.org/10.1361/105497103770330514.

(37)   Bransky, I.; Wimmer, J. M. The High Temperature Defect Structure of CoO. *J. Phys. Chem. Solids* **1972**, *33* (4), 801–812. https://doi.org/https://doi.org/10.1016/S0022-3697(72)80096-9.

(38)   Zunger, A.; Wei, S.-H.; Ferreira, L. G.; Bernard, J. E. Special Quasirandom Structures. *Phys. Rev. Lett.* **1990**, *65* (3), 353–356. https://doi.org/10.1103/PhysRevLett.65.353.

(39)   Aziz, M. J. Film Growth Mechanisms in Pulsed Laser Deposition. *Appl. Phys. A* **2008**, *93* (3), 579. https://doi.org/10.1007/s00339-008-4696-7.

(40)   Song, J. H.; Susaki, T.; Hwang, H. Y. Enhanced Thermodynamic Stability of Epitaxial Oxide Thin Films. *Adv. Mater.* **2008**, *20* (13), 2528–2532. https://doi.org/10.1002/adma.200701919.

(41)   Bae, S. H.; Lee, S. Y.; Kim, H. Y.; Im, S. Comparison of the Optical Properties of ZnO Thin Films Grown on Various Substrates by Pulsed Laser Deposition. *Appl. Surf. Sci.* **2000**, *168* (1–4), 332–334. https://doi.org/10.1016/S0169-4332(00)00781-9.

(42)   Xia, H.; Wan, Y.; Yan, F.; Lu, L. Manganese Oxide Thin Films Prepared by Pulsed Laser Deposition for Thin Film Microbatteries. *Mater. Chem. Phys.* **2014**, *143* (2), 720–727. https://doi.org/10.1016/j.matchemphys.2013.10.005.

(43)   Momma, K.; Izumi, F. VESTA3 for Three-Dimensional Visualization of Crystal, Volumetric and Morphology Data. *J. Appl. Crystallogr.* **2011**, *44* (6), 1272–1276. https://doi.org/10.1107/S0021889811038970.

(44)   Ophus, C.; Ciston, J.; Nelson, C. T. Correcting Nonlinear Drift Distortion of Scanning Probe

and Scanning Transmission Electron Microscopies from Image Pairs with Orthogonal Scan Directions. *Ultramicroscopy* **2016**, *162*, 1–9. https://doi.org/10.1016/j.ultramic.2015.12.002.

(45)   Savitzky, B. H.; Zeltmann, S. E.; Hughes, L. A.; Brown, H. G.; Zhao, S.; Pelz, P. M.; Pekin, T. C.; Barnard, E. S.; Donohue, J.; Rangel Dacosta, L.; Kennedy, E.; Xie, Y.; Janish, M. T.; Schneider, M. M.; Herring, P.; Gopal, C.; Anapolsky, A.; Dhall, R.; Bustillo, K. C.; Ercius, P.; Scott, M. C.; Ciston, J.; Minor, A. M.; Ophus, C. Py4DSTEM: A Software Package for Four-Dimensional Scanning Transmission Electron Microscopy Data Analysis. *Microsc. Microanal.* **2021**, *27* (4), 712–743. https://doi.org/10.1017/S1431927621000477.

(46)   Kresse, G.; Furthmüller, J. Efficient Iterative Schemes for Ab Initio Total-Energy Calculations Using a Plane-Wave Basis Set. *Phys. Rev. B* **1996**, *54* (16), 11169–11186. https://doi.org/10.1103/PhysRevB.54.11169.

(47)   Perdew, J. P.; Ruzsinszky, A.; Csonka, G. I.; Vydrov, O. A.; Scuseria, G. E.; Constantin, L. A.; Zhou, X.; Burke, K. Restoring the Density-Gradient Expansion for Exchange in Solids and Surfaces. *Phys. Rev. Lett.* **2008**, *100* (13), 136406. https://doi.org/10.1103/PhysRevLett.100.136406.

(48)   Dudarev, S. L.; Botton, G. A.; Savrasov, S. Y.; Humphreys, C. J.; Sutton, A. P. Electron-Energy-Loss Spectra and the Structural Stability of Nickel Oxide: An LSDA+U Study. *Phys. Rev. B* **1998**, *57* (3), 1505–1509. https://doi.org/10.1103/PhysRevB.57.1505.

(49)   Zhang, J.; Yan, J.; Calder, S.; Zheng, Q.; McGuire, M. A.; Abernathy, D. L.; Ren, Y.; Lapidus, S. H.; Page, K.; Zheng, H.; Freeland, J. W.; Budai, J. D.; Hermann, R. P. Long-Range Antiferromagnetic Order in a Rocksalt High Entropy Oxide. *Chem. Mater.* **2019**, *31*

(10), 3705–3711. https://doi.org/10.1021/acs.chemmater.9b00624.

(50) Henkelman, G.; Arnaldsson, A.; Jónsson, H. A Fast and Robust Algorithm for Bader Decomposition of Charge Density. *Comput. Mater. Sci.* **2006**, *36* (3), 354–360. https://doi.org/10.1016/j.commatsci.2005.04.010.

(51) Ångqvist, M.; Muñoz, W. A.; Rahm, J. M.; Fransson, E.; Durniak, C.; Rozyczko, P.; Rod, T. H.; Erhart, P. ICET – A Python Library for Constructing and Sampling Alloy Cluster Expansions. *Adv. Theory Simulations* **2019**, *2* (7), 1900015. https://doi.org/10.1002/adts.201900015.